batteries

MDPI

Article

Cu-Substituted $Na_3V_2(PO_4)_3$/C Composites as High-Rate, Long-Cycle Cathodes for Sodium-Ion Batteries

Hyeon-Jun Choi [1,†], Yu Gyeong Kim [2,†], Su Hwan Jeong [3], Sang Jun Lee [3], Young Hwa Jung [4] and Joo-Hyung Kim [1,3,*]

1 Graduate School of Aerospace and Defense Convergence (Materials and Component), Gyeongsang National University (GNU), Jinju 52828, Republic of Korea; chj19gus@gnu.ac.kr
2 School of Material Science and Engineering (Ceramic Engineering), Gyeongsang National University (GNU), Jinju 52828, Republic of Korea; kykkyk021210@gnu.ac.kr
3 Department of Materials Engineering and Convergence Technology, Gyeongsang National University (GNU), Jinju 52828, Republic of Korea; tosil1210@gnu.ac.kr (S.H.J.); tkdwns1008@gnu.ac.kr (S.J.L.)
4 PLS-II Beamline Division, Pohang Accelerator Laboratory (PAL), Pohang 37673, Republic of Korea; yhjung@postech.ac.kr
* Correspondence: kimjoohyung@gnu.ac.kr; Tel.: +82-55-772-1685
† These authors contributed equally to this work.

Abstract

The advancement of high-performance sodium-ion batteries (SIBs) necessitates cathode materials that exhibit both structural robustness and long-term electrochemical stability. $Na_3V_2(PO_4)_3$ (NVP), with its NASICON-type framework, is a promising candidate; however, its inherently low electronic conductivity restricts full capacity utilization. In this study, carbon-coated and Cu-substituted $Na_3V_2(PO_4)_3$ (NVCP) composites were synthesized via a solid-state reaction using agarose as a carbon source. Structural and morphological analyses confirmed the successful incorporation of Cu^{2+} ions into the rhombohedral lattice without disrupting the crystal structure and the formation of uniform conductive carbon layers. The substitution of Cu^{2+} induced increased carbon disorder and partial oxidation of V^{3+} to V^{4+}, contributing to enhanced electronic conductivity. Consequently, NVCP exhibited excellent long-term cycling performance, maintaining over 99% of its initial capacity after 500 cycles at 0.5 C. Furthermore, the electrode demonstrated outstanding high-rate capabilities, with a capacity recovery of 97.98% after cycling at 20 C and returning to lower current densities. These findings demonstrate that Cu substitution combined with carbon coating synergistically enhances structural integrity and Na^+ transport, offering an effective approach to engineer high-performance cathodes for next-generation SIBs.

Keywords: sodium-ion batteries; $Na_3V_2(PO_4)_3$; cathode; substitution; carbon coating

Academic Editors: Diana Golodnitsky and Zhenbo Wang

Received: 25 May 2025
Revised: 14 July 2025
Accepted: 5 August 2025
Published: 11 August 2025

Citation: Choi, H.-J.; Kim, Y.G.; Jeong, S.H.; Lee, S.J.; Jung, Y.H.; Kim, J.-H. Cu-Substituted $Na_3V_2(PO_4)_3$/C Composites as High-Rate, Long-Cycle Cathodes for Sodium-Ion Batteries. *Batteries* **2025**, *11*, 308. https://doi.org/10.3390/batteries11080308

1. Introduction

The global transition toward sustainable development has driven the growing demand for efficient, low-cost, and environmentally friendly energy storage systems. Lithium-ion batteries (LIBs) have long been the dominant technology in portable electronics and electric vehicles (EVs) owing to their high energy density and long cycle life. However, the reliance of LIBs on critical but limited elements in the Earth's crust, such as lithium, cobalt, and nickel, has raised concerns regarding long-term supply stability, cost volatility, and environmental sustainability [1–3]. These challenges have prompted intensive research into alternative chemistries that can offer comparable performance while utilizing more abundant and safer raw materials.

Sodium-ion batteries (SIBs) have emerged as a promising alternative due to the abundance, low cost, and wide geographic distribution of sodium resources [2,4]. SIBs operate through an intercalation mechanism similar to that of LIBs, enabling compatibility with existing manufacturing infrastructure [1]. In particular, they are well suited for stationary energy storage applications, where cost-effectiveness, cycle life, and environmental considerations are prioritized over energy density [5–10]. Among various cathode candidates, polyanionic compounds with a NASICON (Na super ionic conductor) structure have attracted considerable attention due to their intrinsic thermal stability, high operating voltage, and robust three-dimensional frameworks [11]. A representative example, $Na_3V_2(PO_4)_3$ (NVP), features a stable structure composed of corner-sharing VO_6 octahedra and PO_4 tetrahedra, forming wide diffusion channels conducive to rapid Na^+ transport [12–14]. Its excellent cyclability, rate performance, and voltage stability under diverse conditions have made it a benchmark cathode material [15,16].

Despite these advantages, the practical performance of NVP is hampered by its low intrinsic electronic conductivity (~10^{-8} S cm^{-1}), which limits its rate capability and the full utilization of its theoretical capacity [17–19]. To address this issue, several modification strategies have been explored, including conductive carbon coating, nanostructuring, and elemental doping. Among them, carbon coating is widely employed to form interconnected conductive networks that enhance electron transport and maintain structural integrity during cycling [20,21]. Simultaneously, substitutional doping of vanadium with aliovalent (e.g., Mg^{2+}, Mn^{2+}, and Ti^{4+}) or isovalent (e.g., Cr^{3+}, Ru^{3+}, and Y^{3+}) transition metals has proven effective in modulating the electronic structure, stabilizing the lattice, and facilitating Na^+ diffusion kinetics [8,13,18,22–24]. In particular, Cu^{2+} doping has shown promising effects by introducing hole carriers and increasing the proportion of electroactive V^{4+} species, which collectively contribute to reduced charge-transfer resistance while maintaining the integrity of the NASICON framework [25,26]. In addition, the partial substitution of V^{4+} with Cu^{2+} may lead to the formation of local structural distortions, which can facilitate enhanced electronic conduction and potentially improve Na^+ diffusion through the three-dimensional channels [27–29]. Furthermore, the inherent structural openness of the NASICON framework contributes to lower activation barriers for Na^+ migration, while defect engineering strategies such as vacancy formation offer additional diffusion pathways [27–30]. In this study, we synthesized $Na_3V_2(PO_4)_3$/C (NVP) and Cu-substituted $Na_3V_{1.9}Cu_{0.1}(PO_4)_3$/C (NVCP) composites via a simple and scalable solid-state method. Agarose was employed as a multifunctional carbon feedstock and shape-controlling agent to enable conductive carbon coating and particle size refinement [21]. This environmentally benign biopolymer also facilitates interparticle connectivity upon thermal treatment. The effectiveness of agarose as a carbon precursor is further supported by previous work demonstrating its role in producing uniform and conductive carbon coatings with strong interfacial adhesion, thereby improving structural integrity and cycling stability [31]. A fixed Cu content (x = 0.1) was selected to partially replace V^{3+} ions in the NASICON lattice, which introduces hole carriers, increases the proportion of V^{4+}, and enhances electronic conductivity. This aliovalent substitution is also expected to stabilize the framework and improve Na^+ extraction/insertion behavior and diffusion kinetics [29]. The final composites were optimized through ball milling and controlled thermal processing to further enhance structural uniformity and electrochemical performance.

2. Materials and Methods

2.1. Material Synthesis

$Na_3V_2(PO_4)_3$/C and $Na_3V_{1.9}Cu_{0.1}(PO_4)_3$/C composites were synthesized using a solid-state method. Stoichiometric amounts of NH_4VO_3, NaH_2PO_4, CuO(II), and agarose

were mixed and ball-milled in ethanol for 24 h to form a homogeneous slurry. Subsequently, the ethanol was evaporated by stirring at approximately 80 °C to obtain a precursor powder. The powder was then calcined under an Ar/H_2 (v/v = 9.3:0.7) atmosphere: first at 650 °C for 6 h and subsequently at 850 °C for 8 h, obtaining the final NVP and NVCP samples.

2.2. Material Characterization

Phase identification was carried out using an X-ray diffraction device (XRD, Bruker, D8 Advance A25 Plus, Jinju, Republic of Korea) at a scan rate of 4.0 min^{-1} over a 2θ range of 10–60°. Field-emission scanning electron microscopy (FE-SEM, JEOL, JSM-7610F, Jinju, Republic of Korea) and transmission electron microscopy (TEM, Tecnai, G2 F30, Jinju, Republic of Korea) were employed to observe the morphology and microstructure of the samples. X-ray photoelectron spectroscopy (XPS, Thermo Fisher Scientific, K-Alpha$^+$, Jinju, Republic of Korea) was utilized to determine the oxidation states of vanadium. Quantitative elemental analysis (Na, P, V, and Cu) was performed using inductively coupled plasma optical emission spectrometry (ICP-OES, iCAP 6300, Thermofisher Scientific, Daejeon, Republic of Korea). Raman spectroscopy (RAMAN, Nanophoton, RAMAN touch, Jinju, Republic of Korea) and a micro automated elemental analyzer (m-EA, TrueSpec Micro CHNS, Jinju, Republic of Korea) were employed to analyze the carbon structure and content.

2.3. Electrochemical Measurements

Electrochemical properties were examined using CR2032 half coin-type cells assembled in an argon-filled glove box. The cathodes were prepared by mixing the active material, ketjen black (KB), and polyvinylidene fluoride (PVDF) at a weight ratio of 8:1:1 using N-methyl-2-pyrrolidone (NMP) as the solvent. The slurry was uniformly applied to the Al foil at a thickness of 150 μm and vacuum dried at 80 °C for at least one day. Subsequently, the dried foil was punched into disc shapes with a diameter of 12 mm to fabricate the electrodes. The assembled cell featured a sodium metal anode, a GF/D separator, and an electrolyte of 1 M $NaPF_6$ in ethylene carbonate (EC) and diethyl carbonate (DEC) (v/v = 1:1) with 5 wt% fluorinated ethylene carbonate (FEC). The galvanostatic charge and discharge measurements, cyclic voltammetry (CV), and galvanostatic intermittent titration technique (GITT) investigations were conducted using a WonATech (WBCS3000 L, WonATech, Sunnyvale, CA, USA) and NEWARE (MIHW-200-160CH-B, NEWARE, Shenzhen, China) battery cycler with a voltage range of 2.2–4.2 V, and the electrochemical impedance copy was conducted using a Potentiostat (VSP-3e, BioLogic, Seyssinet-Pariset, France).

3. Results and Discussion

3.1. Structural and Morphological Characterization

Figure 1 shows the X-ray diffraction (XRD) patterns of $Na_3V_2(PO_4)_3/C$ (NVP) and Cu^{2+}-substituted $Na_3V_{1.9}Cu_{0.1}(PO_4)_3/C$ (NVCP) samples. All major diffraction peaks in both patterns can be indexed to the rhombohedral NASICON-type structure (space group R-3c), consistent with the standard pattern (COD ID: 2225132) [32], indicating successful formation of the target phase [12,14]. Notably, small impurity peaks around 2θ ≈ 13° and 2θ ≈ 34° indicated with (*) were detected in the NVP sample, which were absent in the NVCP sample. This suggests that the introduction of Cu^{2+} ions into the lattice promotes phase purity and suppresses the formation of secondary phases, such as $NaPO_3$, P, or $Na_4P_2O_7$, which are frequently observed as byproducts during high-temperature solid-state synthesis and may contribute to the formation of a thermodynamically more stable single-phase product under high-temperature solid-state synthesis conditions [8]. Additionally, subtle shifts in diffraction peak positions toward lower 2θ angles were observed for

NVCP compared to NVP. This shift is attributed to the partial substitution of V^{3+} (ionic radius ≈ 0.64 Å) with slightly larger Cu^{2+} ions (≈0.73 Å), which leads to lattice expansion. Therefore, the assumption that Cu doping, as an alovalent element, may alter the local charge balance and act as a pillar to suppress phase separation or defect accumulation during crystallization, thereby promoting the formation of a structurally consistent NASICON framework, is reasonable [26]. Such structural modification is beneficial for enhancing Na^+ diffusion pathways, as the widened channels can facilitate ion transport and mitigate strain during (de)intercalation processes [25,33]. Moreover, the intensity of several peaks in the NVCP pattern appears sharper and more well-defined than those of the undoped NVP, indicating improved crystallinity. In polyanion systems, low-concentration doping has been shown to enhance crystallinity, reduce grain boundary resistance, and thereby improve Na^+ diffusion and charge transfer kinetics, ultimately resulting in superior rate performance and cycle life compared to undoped NVP [34]. In NASICON-type polyanion frameworks, a balance between structural order and defect chemistry plays a crucial role in determining electrochemical performance. While excessive disorder may impede ion transport and structural stability, appropriately regulated certain types of localized defects can facilitate Na^+ diffusion or enhance electronic conductivity [35,36]. Therefore, optimizing crystallinity through controlled doping not only improves long-range ion transport by reducing grain boundary resistance but also helps modulate the formation of functional defects that contribute positively to charge transport kinetics and cycling stability. These effects collectively suggest that Cu^{2+} substitution not only preserves the structural stability of the NASICON framework but also promotes phase purity and favorable lattice modulation—factors that contribute to the enhanced electrochemical performance observed in the doped material.

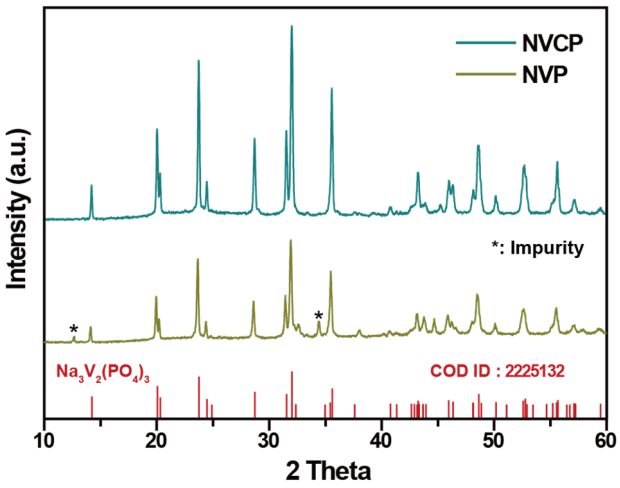

Figure 1. XRD patterns of NVCP and NVP.

Morphological and microstructural characterization of pristine NVP and NVCP samples is shown in Figure 2. The SEM images (Figure 2a,b) reveal that both materials possess a bulk-type morphology consisting of aggregated primary particles. The particles exhibit irregular shapes with a wide size distribution, and numerous smaller secondary particles are found attached to the surface of larger grains. This multiscale aggregation may contribute to enhanced electronic and ionic connectivity by increasing contact interfaces, as nanoparticle aggregation has been reported to promote electrolyte penetration and ion diffusion through expanded surface areas [7]. High-resolution TEM (HRTEM) images (Figure 2c,f) clearly show the presence of an amorphous carbon coating layer on the surface of both NVP and NVCP particles. The carbon layer originates from the pyrolysis of agarose, a renewable biopolymer employed as the carbon source. Such coatings are known to suppress surface reactions, enhance electronic conductivity, and buffer structural strain

during cycling [21,25,37]. Selected Area Electron Diffraction (SAED) patterns (Figure 2d,e for NVCP and Figure 2g,h for NVP) exhibit clear diffraction spots with ring-like features, confirming the polycrystalline nature and good crystallinity of both samples. No significant differences in diffraction symmetry were observed between the two, indicating that Cu^{2+} substitution did not alter the long-range NASICON phase structure. Energy-dispersive X-ray spectroscopy (EDS) elemental mapping (Figure 2i,j) further confirms the homogeneous distribution of constituent elements (Na, V, P, O, and C), and importantly, Cu is uniformly incorporated into the NVCP structure without visible phase separation. This supports the successful substitution of V^{3+} with Cu^{2+} ions within the NASICON framework [25,26]. The uniform carbon distribution throughout the particle surface additionally corroborates the effectiveness of the agarose-based coating.

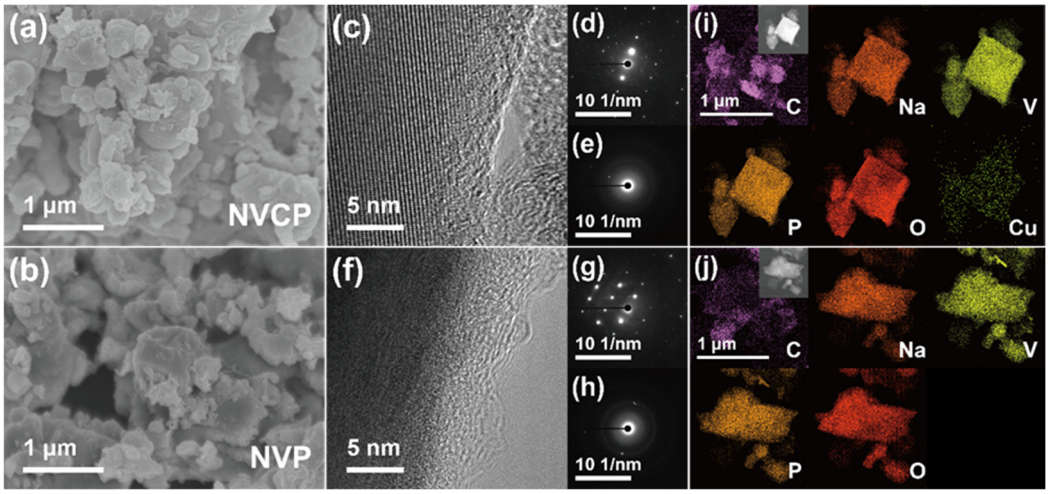

Figure 2. SEM images of (**a**) NVCP and (**b**) NVP. TEM images of NVCP; (**c**) HRTEM and (**d**,**e**) SAED images. TEM images of NVP; (**f**) HRTEM and (**g**,**h**) SAED images. EDS mapping images of (**i**) NVCP and (**j**) NVP; C, Na, V, P, O, and Cu elements.

Raman spectra of pristine NVP and NVCP samples, providing insights into the structural properties of the coated carbon layers, are shown in Figure 3a. Both spectra display two characteristic peaks located at approximately 1361.6 cm^{-1} and 1606.3 cm^{-1}, corresponding to the D band (disordered sp^3 carbon) and the G band (graphitic sp^2 carbon), respectively [17]. The intensity ratio of these two peaks (I_D/I_G) is often employed to evaluate the degree of disorder and defect density within the carbonaceous structure [38]. The calculated I_D/I_G ratio is 1.1875 for NVCP, higher than 0.9591 for NVP, suggesting that Cu substitution leads to a greater degree of disorder in the carbon coating. To further investigate the relationship between carbon structure and electronic conductivity, micro-elemental analysis (m-EA) was conducted. The results showed that NVCP has a higher carbon content of 17.21% compared to 15.25% for NVP, indicating the formation of a thicker and more continuous carbon coating layer. Interestingly, a higher degree of disorder can enhance electronic conductivity by introducing more active sites and hopping pathways for electron transport [29,38]. This is particularly beneficial in NASICON-type structures where bulk ionic conductivity is high but electronic conductivity tends to be low [5]. Similar correlations between disorder degree and enhanced conductivity have been systematically studied in carbon-based materials such as CNx nanotubes, highlighting the critical role of defect engineering [38]. Thus, disordered carbon coatings complement the intrinsic ionic conduction channels of $Na_3V_2(PO_4)_3$ by facilitating faster electronic transport.

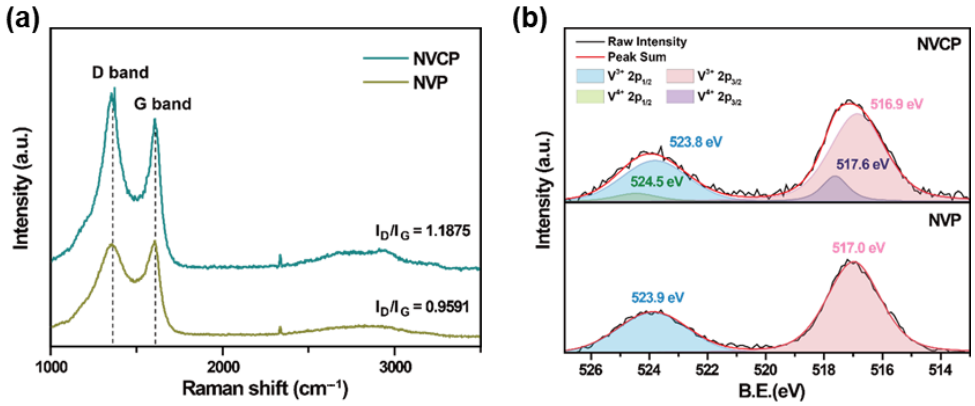

Figure 3. (**a**) Raman spectra and (**b**) V 2p XPS spectra of NVCP and NVP, respectively.

Figure 3b presents the XPS spectra of the V 2p region for pristine NVP and NVCP samples, offering insights into the vanadium oxidation states and the effects of Cu substitution on the electronic environment. For the NVP sample, two well-defined peaks centered at 517.0 eV and 523.9 eV correspond to the V^{3+} $2p_3/_2$ and $2p_1/_2$ spin–orbit split components, respectively, characteristic of vanadium in the +3 oxidation state [18,39]. This observation is consistent with the expected oxidation state of V in the NASICON-type $Na_3V_2(PO_4)_3$ structure. After Cu^{2+} substitution, the NVCP sample exhibits noticeable peak broadening and the development of a distinct shoulder on the higher binding energy side of the main peaks. This asymmetric feature is attributed to the emergence of V^{4+} species, indicating partial oxidation of V^{3+} induced by Cu substitution [18,26,34]. The charge imbalance introduced by aliovalent Cu^{2+} substitution likely triggers partial oxidation of adjacent vanadium ions from V^{3+} to V^{4+} to maintain overall charge neutrality [8]. The generation of V^{4+} not only modifies the electronic structure of the host lattice but also has important electrochemical implications. Partial oxidation of transition metals upon aliovalent substitution has also been observed in other phosphate frameworks, reflecting general trends in defect-compensated electronic structure tuning [18,34]. Such redox flexibility provides additional active sites for sodium (de)intercalation, potentially boosting specific capacity and rate capability [11].

3.2. Electrochemical Performance

Cyclic voltammetry (CV) curves for NVP and Cu^{2+}-substituted NVCP electrodes measured at a scan rate of 0.1 mV s^{-1} within the voltage range of 2.2–4.2 V are shown in Figure 4. Both materials exhibit typical redox peaks associated with the V^{3+}/V^{4+} redox couple [29,33]. The $Na_3V_2(PO_4)_3$ NASICON structure contains two distinct Na^+ crystallographic sites, labeled Na1 and Na2. Due to its relatively open and less constrained environment, the Na(2) site preferentially participates in reversible Na^+ extraction/insertion during electrochemical cycling [11,40,41]. At the CV curves, the clear anodic peak corresponds to the simultaneous extraction of two sodium ions from the Na(2) sites, while the presence of two cathodic peaks around ~3.3 V is consistent with a two-step reinsertion mechanism involving energetically distinct Na sites. Na^+ ions initially insert into the more electrochemically active Na(2) sites, followed by a concerted site exchange process involving Na(1) sites with a lower energy barrier, thereby supporting the origin of double cathodic peaks observed in the CV profiles [42]. Notably, the enhanced peak intensity and reduced overpotential between the oxidative and reductive peaks in NVCP suggest improved reversibility and possibly lower activation barriers induced by Cu^{2+} doping [5,29]. In addition, the intensity change of the reductive peaks between the 1st and 10th cycles in NVCP suggests progressive structural rearrangements associated with Na^+ reinsertion pathways, likely promoted by Cu^{2+}-induced lattice expansion and charge-compensation effects that enhance ionic

diffusion. This behavior is notably less pronounced in undoped NVP, indicating the role of aliovalent substitution in facilitating such structural evolution [6,11,22]. As shown in the GITT profiles, the NVCP sample exhibits smaller overpotential (ΔE_t) and faster voltage stabilization after each current pulse, indicating enhanced Na^+ diffusivity and reduced internal resistance. The smoother voltage relaxation behavior and more consistent ΔE_S values in NVCP further suggest that Cu^{2+} doping facilitates more uniform Na^+ migration pathways and stabilizes the host structure. In particular, although the overpotential at the 3.2 V plateau Na(1) sites is slightly larger than that at the 3.3 V plateau Na(2) sites during the insertion process, stable insertion is observed until the end of discharge. This is believed to be due to structural rearrangement through a concerted ion-exchange process. These observations suggest that Cu^{2+} substitution improves interfacial charge transport and preserves structural stability, contributing to sustained Na^+ diffusion pathways and mitigating interfacial degradation over extended cycling.

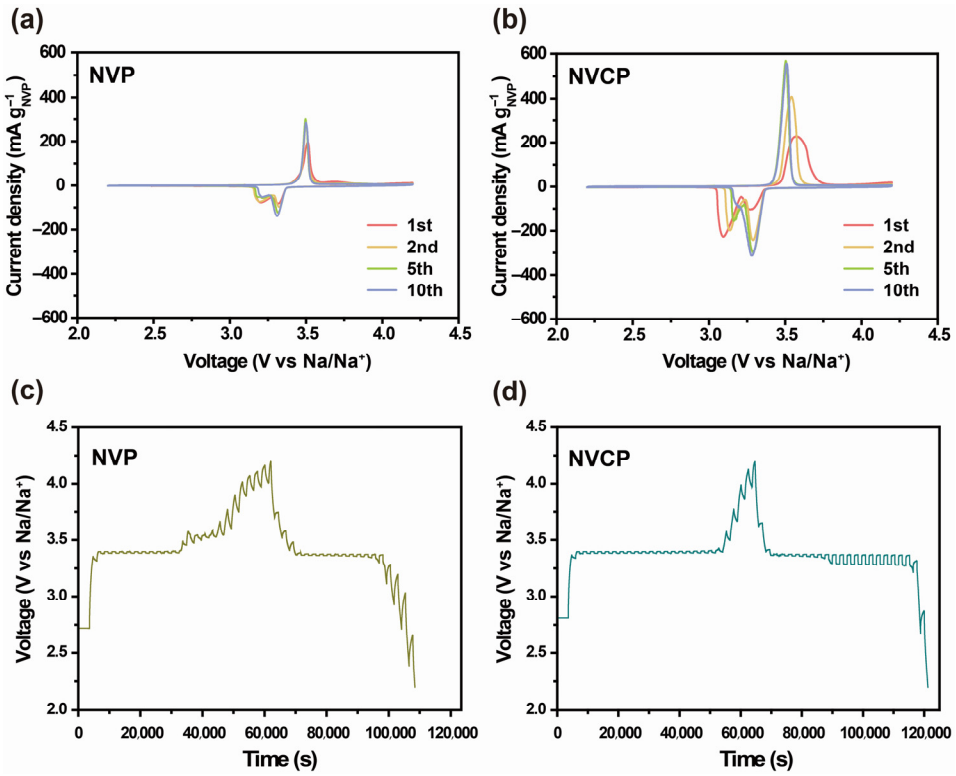

Figure 4. CV and GITT curves of (**a**,**c**) NVP and (**b**,**d**) NVCP.

Figure 5 illustrates the long-term cycling performance and charge–discharge behavior of NVP and NVCP at 0.5 C. The initial discharge capacities are 92.37 mA h g^{-1} for NVP and 107.53 mA h g^{-1} for NVCP, with both samples retaining over 99% of their initial capacity after 500 cycles, indicating minimal irreversible side reactions during cycling [19,20,43]. In the EIS spectra, the Nyquist plots of both NVP and NVCP electrodes were measured in the frequency range of 1 MHz to 100 mHz. Although the fitted charge transfer resistance (R_{ct}) value of pristine NVP is initially slightly lower than that of NVCP, the Cu-doped NVCP electrode exhibits more stable impedance behavior after cycling. In particular, the increase in R_{ct} and Warburg impedance is much smaller in NVCP than in NVP, indicating that Cu^{2+} substitution helps suppress interfacial degradation and maintain Na^+ transport kinetics over long-term cycling. The corresponding equivalent circuits for the fitting are shown in the inset. Both materials exhibit a flat voltage plateau around 3.4 V, which corresponds to the reversible two-Na-ion extraction/insertion mechanism at the Na(2) sites within the NASICON structure [20,33]. Interestingly, NVCP displays a distinct staircase feature

near 3.2 V in the initial charge–discharge cycles. This feature gradually diminishes with subsequent cycles, signifying a kinetic hindrance and structural rearrangement within the Na^+ diffusion pathways during early cycling. Cu^{2+} substitution facilitates these rearrangements by expanding the lattice and improving the ionic transport kinetics. This dopant-induced lattice expansion and subsequent improved kinetics significantly reduce the internal resistance, thereby stabilizing the electrochemical reactions during repeated Na-ion insertion/extraction.

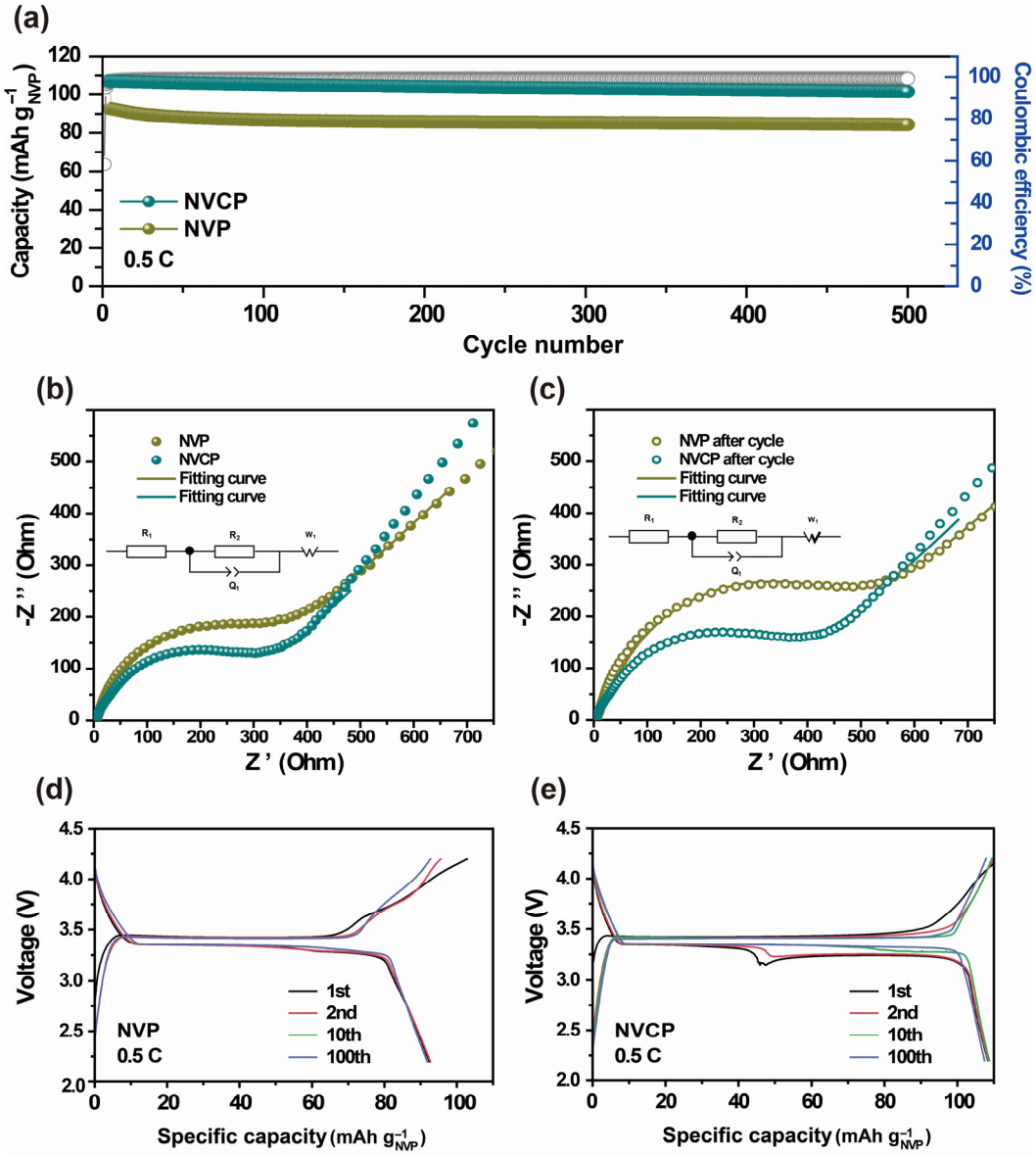

Figure 5. (**a**) Cycling performance of NVP and NVCP at 0.5 C; electrochemical impedance spectra (EIS) of NVP and NVCP (**b**) before and (**c**) after cycling; galvanostatic charge–discharge profiles of (**d**) NVP and (**e**) NVCP at 0.5 C.

Figure 6 shows the rate capability of NVP and NVCP over a wide range of current densities from 0.1 C to 20 C. Both electrodes exhibit the typical trend of decreasing discharge capacity with increasing current density, reflecting inherent limitations in sodium-ion diffusion kinetics at higher C-rates. At 0.1 C to 20 C, NVP exhibits discharge capacities of 98.9, 88.8, 85.3, 82.4, 77.9, 72.8, and 64.1 mA h g^{-1}, whereas NVCP shows significantly higher values of 111.3, 109.0, 108.0, 106.5, 102.7, 97.6, and 89.0 mA h g^{-1}, respectively. After the high-rate cycling tests, when the current rate is returned to 0.5 C, NVCP recovers

approximately 97.98% of its initial capacity, whereas NVP recovers only about 90.01%. This superior rate performance and excellent capacity recovery in NVCP are attributed to enhanced structural robustness and faster Na^+ ion diffusion, made possible by Cu^{2+}-induced lattice expansion and defect engineering [5,14].

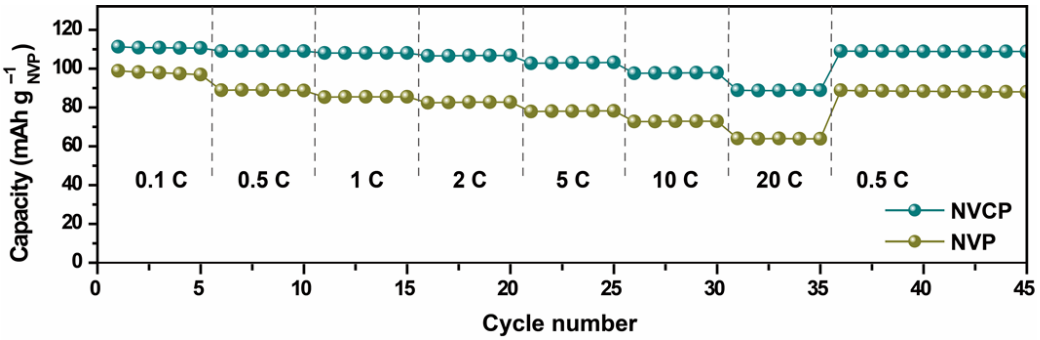

Figure 6. Rate performance of NVCP and NVP.

4. Conclusions

In this study, $Na_3V_{1.9}Cu_{0.1}(PO_4)_3/C$ (NVCP) composites were successfully synthesized via a solid-state method and evaluated as a cathode material for sodium-ion batteries (SIBs). Compared to conventional $Na_3V_2(PO_4)_3/C$ (NVP), NVCP exhibited enhanced electrochemical properties, particularly demonstrating improved electronic conductivity and a stable NASICON structure through Cu substitution. XRD and SEM/TEM analyses verified the crystalline and microstructural characteristics of NVCP, while XPS analysis revealed the oxidation state changes of vanadium (V). NVCP provided a stable voltage plateau at 3.4 V after structural rearrangement by V^{3+}/V^{4+} redox reactions, showing high reversibility. The electrochemical performance evaluation indicated that NVCP provided an initial capacity of 107.53 mA h g^{-1} at 0.5 C, maintaining over 99% of its initial capacity even after 500 cycles. In addition, NVCP demonstrated an excellent discharge capacity of 89.0 mA h g^{-1} at a high charge/discharge rate of 20 C, along with a high performance recovery rate of 97.98% when subsequently cycled back to 0.5 C. This remarkable performance is attributed to the enhanced Na-ion insertion/extraction process and improved structural stability facilitated by Cu substitution. In conclusion, this study has confirmed the outstanding electrochemical performance and long cycle life of $Na_3V_{1.9}Cu_{0.1}(PO_4)_3/C$, highlighting its potential as a promising cathode material for high-performance SIBs.

Author Contributions: Conceptualization, H.-J.C. and Y.G.K.; methodology, H.-J.C. and Y.G.K.; validation, H.-J.C., Y.G.K., S.H.J. and S.J.L.; formal analysis, H.-J.C. and Y.G.K.; investigation, H.-J.C. and Y.G.K.; resources, J.-H.K.; data curation, H.-J.C. and Y.G.K.; writing—original draft preparation, H.-J.C. and Y.G.K.; writing—review and editing, H.-J.C. and J.-H.K.; supervision, Y.H.J. and J.-H.K.; project administration, J.-H.K.; funding acquisition, J.-H.K. All authors have read and agreed to the published version of the manuscript.

Funding: This work was supported by the Research Resurgence under the Glocal University 30 Project at Gyeongsang National University in 2024.

Data Availability Statement: The original contributions presented in the study are included in the article. Further inquiries can be directed to the corresponding author.

Conflicts of Interest: The authors declare no conflicts of interest.

References

1. Hwang, J.Y.; Myung, S.T.; Sun, Y.K. Sodium-ion batteries: Present and future. *Chem. Soc. Rev.* **2017**, *46*, 3529–3614. [CrossRef]
2. Yabuuchi, N.; Kubota, K.; Dahbi, M.; Komaba, S. Research Development on Sodium-Ion Batteries. *Chem. Rev.* **2014**, *114*, 11636–11682. [CrossRef]
3. Goodenough, J.B.; Kim, Y. Challenges for Rechargeable Li Batteries. *Chem. Mat.* **2009**, *22*, 587–603. [CrossRef]
4. Zeng, X.; Peng, J.; Guo, Y.; Zhu, H.; Huang, X. Research Progress on $Na_3V_2(PO_4)_3$ Cathode Material of Sodium Ion Battery. *Front. Chem.* **2020**, *8*, 635. [CrossRef] [PubMed]
5. Zhang, B.; Ma, K.; Lv, X.; Shi, K.; Wang, Y.; Nian, Z.; Li, Y.; Wang, L.; Dai, L.; He, Z. Recent advances of NASICON-$Na_3V_2(PO_4)_3$ as cathode for sodium-ion batteries: Synthesis, modifications, and perspectives. *J. Alloy. Compd.* **2021**, *867*, 159060. [CrossRef]
6. Hu, J.; Li, X.; Liang, Q.; Xu, L.; Ding, C.; Liu, Y.; Gao, Y. Optimization Strategies of $Na_3V_2(PO_4)_3$ Cathode Materials for Sodium-Ion Batteries. *Nano-Micro Lett.* **2024**, *17*, 33. [CrossRef]
7. Wang, M.; Huang, X.; Wang, H.; Zhou, T.; Xie, H.; Ren, Y. Synthesis and electrochemical performances of $Na_3V_2(PO_4)_2F_3$/C composites as cathode materials for sodium ion batteries. *RSC Adv.* **2019**, *9*, 30628–30636. [CrossRef]
8. Bag, S.; Murarka, H.; Zhou, C.; Bhattacharya, A.; Jokhakar, D.; Pol, V.G.; Thangadurai, V. Understanding the Na-Ion Storage Mechanism in $Na_{3+x}V_{2-x}M_x(PO_4)_3$ (M = Ni^{2+}, Co^{2+}, Mg^{2+}; x = 0.1–0.5) Cathodes. *ACS Appl. Energ. Mater.* **2020**, *3*, 8475–8486. [CrossRef]
9. Cushing, B.L.; Goodenough, J.B. $Li_2NaV_2(PO_4)_3$: A 3.7 V Lithium-Insertion Cathode with the Rhombohedral NASICON Structure. *J. Solid State Chem.* **2001**, *162*, 176–181. [CrossRef]
10. Du, K.; Guo, H.; Hu, G.; Peng, Z.; Cao, Y. $Na_3V_2(PO_4)_3$ as cathode material for hybrid lithium ion batteries. *J. Power Sources* **2013**, *223*, 284–288. [CrossRef]
11. Masquelier, C.; Croguennec, L. Polyanionic (Phosphates, Silicates, Sulfates) Frameworks as Electrode Materials for Rechargeable Li (or Na) Batteries. *Chem. Rev.* **2013**, *113*, 6552–6591. [CrossRef]
12. Jian, Z.; Yuan, C.; Han, W.; Lu, X.; Gu, L.; Xi, X.; Hu, Y.S.; Li, H.; Chen, W.; Chen, D.; et al. Atomic Structure and Kinetics of NASICON $Na_xV_2(PO_4)_3$ Cathode for Sodium-Ion Batteries. *Adv. Funct. Mater.* **2014**, *24*, 4265–4272. [CrossRef]
13. Zhou, T.; Chen, Y. Heterojunction of Y^{3+}-substituted $Na_3V_2(PO_4)_3$-$NaYO_2$ accelerating kinetics with superior performance for full sodium-ion batteries. *J. Colloid Interface Sci.* **2024**, *654*, 1163–1176. [CrossRef]
14. Lalère, F.; Seznec, V.; Courty, M.; David, R.; Chotard, J.N.; Masquelier, C. Improving the energy density of $Na_3V_2(PO_4)_3$-based positive electrodes through V/Al substitution. *J. Mater. Chem. A* **2015**, *3*, 16198–16205. [CrossRef]
15. Akçay, T.; Häringer, M.; Pfeifer, K.; Anhalt, J.; Binder, J.R.; Dsoke, S.; Kramer, D.; Mönig, R. $Na_3V_2(PO_4)_3$—A Highly Promising Anode and Cathode Material for Sodium-Ion Batteries. *ACS Appl. Energ. Mater.* **2021**, *4*, 12688–12695. [CrossRef]
16. Jian, Z.; Han, W.; Lu, X.; Yang, H.; Hu, Y.S.; Zhou, J.; Zhou, Z.; Li, J.; Chen, W.; Chen, D.; et al. Superior Electrochemical Performance and Storage Mechanism of $Na_3V_2(PO_4)_3$ Cathode for Room-Temperature Sodium-Ion Batteries. *Adv. Energy Mater.* **2012**, *3*, 156–160. [CrossRef]
17. Duan, W.; Zhu, Z.; Li, H.; Hu, Z.; Zhang, K.; Cheng, F.; Chen, J. $Na_3V_2(PO_4)_3$@C core–shell nanocomposites for rechargeable sodium-ion batteries. *J. Mater. Chem. A* **2014**, *2*, 8668–8675. [CrossRef]
18. Fang, J.; Wang, S.; Yao, X.; Hu, X.; Wang, Y.; Wang, H. Ration design of porous Mn-doped $Na_3V_2(PO_4)_3$ cathode for high rate and super stable sodium-ion batteries. *Electrochim. Acta* **2019**, *295*, 262–269. [CrossRef]
19. Ghosh, S.; Barman, N.; Patra, B.; Senguttuvan, P. Structural and Electrochemical Sodium (De)intercalation Properties of Carbon-Coated NASICON-$Na_{3+y}V_{2-y}Mn_y(PO_4)_3$ Cathodes for Na-Ion Batteries. *Adv. Energy Sustain. Res.* **2022**, *3*, 2200081. [CrossRef]
20. Jian, Z.; Zhao, L.; Pan, H.; Hu, Y.-S.; Li, H.; Chen, W.; Chen, L. Carbon coated $Na_3V_2(PO_4)_3$ as novel electrode material for sodium ion batteries. *Electrochem. Commun.* **2012**, *14*, 86–89. [CrossRef]
21. Feng, P.; Wang, W.; Wang, K.; Cheng, S.; Jiang, K. $Na_3V_2(PO_4)_3$/C synthesized by a facile solid-phase method assisted with agarose as a high-performance cathode for sodium-ion batteries. *J. Mater. Chem. A* **2017**, *5*, 10261–10268. [CrossRef]
22. Huang, Y.; Li, X.; Wang, J.; Miao, L.; Li, C.; Han, J.; Huang, Y. Superior Na-ion storage achieved by Ti substitution in $Na_3V_2(PO_4)_3$. *Energy Storage Mater.* **2018**, *15*, 108–115. [CrossRef]
23. Mai, B.; Xing, B.; Yue, Y.; Cai, N.; Cai, C.; Lian, S.; Fan, H.; Yan, M.; Zhu, T.; Hu, P.; et al. Cr-doped $Na_3V_2(PO_4)_3$@C enables high-capacity with V2+/V5+ reaction and stable sodium storage. *J. Mater. Sci. Technol.* **2023**, *165*, 1–7. [CrossRef]
24. Shi, H.; Guo, L.; Chen, Y. Unraveling the modified mechanism of ruthenium substitution on $Na_3V_2(PO_4)_3$ with superior rate capability and ultralong cyclic performance. *J. Colloid Interface Sci.* **2024**, *664*, 487–499. [CrossRef]
25. Lv, Z.Q.; Zhang, Y.L.; Liu, Z.Q.; Qi, X.; Xu, Y.B.; Cui, Y.M.; Xu, W.L.; Yang, Z.L.; Zheng, Q. Carbon coated $Na_{3+x}V_{2-x}Cu_x(PO_4)_3$@C cathode for high-performance sodium ion batteries. *J. Colloid Interface Sci.* **2024**, *666*, 540–546. [CrossRef]
26. Peng, Z.; Chen, B.; Yu, S.; Wu, K.; Zhang, F.; Gao, P. Cu^{2+} substitution regulating $Na_3V_2(PO_4)_3$ with solid SEI membrane for superior electrochemical performance. *Dalton Trans.* **2025**, *54*, 4743–4754. [CrossRef] [PubMed]
27. Song, W.; Ji, X.; Wu, Z.; Zhu, Y.; Yang, Y.; Chen, J.; Jing, M.; Li, F.; Banks, C.E. First exploration of Na-ion migration pathways in the NASICON structure $Na_3V_2(PO_4)_3$. *J. Mater. Chem. A* **2014**, *2*, 5358–5362. [CrossRef]

28. Ragul, S.; Prabakaran, A.; Sujithkrishnan, E.; Kannadasan, K.; Elumalai, P. Sodium-ion battery using a NASICON-type $Na_3V_2(PO_4)_3$ cathode: Quantification of diffusive and capacitive Na^+ charge storage. *New J. Chem.* **2024**, *48*, 12323–12335. [CrossRef]
29. Zhang, D.; Feng, P.; Xu, B.; Li, Z.; Qiao, J.; Zhou, J.; Chang, C. High Rate Performance of $Na_3V_{2-x}Cu_x(PO_4)_3$/C Cathodes for Sodium Ion Batteries. *J. Electrochem. Soc.* **2017**, *164*, A3563–A3569. [CrossRef]
30. Cong, J.; Luo, S.-h.; Li, P.; Li, K.; Li, P.; Yan, S.; Qian, L.; Liu, X. Ultracapacity Properties of the Refined Structure in Na-Rich $Na_{3.4}V_2(PO_4)_3$/C as Sodium-Ion Battery Cathodes by Tapping the Na-Vacancy Potential. *ACS Sustain. Chem. Eng.* **2023**, *11*, 16341–16353. [CrossRef]
31. Hwang, G.; Kim, J.M.; Hong, D.; Kim, C.K.; Choi, N.S.; Lee, S.Y.; Park, S. Multifunctional natural agarose as an alternative material for high-performance rechargeable lithium-ion batteries. *Green Chem.* **2016**, *18*, 2710–2716. [CrossRef]
32. Xiong, W.; Tu, Z.; Yin, Z.; Zhang, X.; Hu, X.; Wu, Y. Supported Ionic Liquid Gel Membranes Enhanced by Ionization Modification for Sodium Metal Batteries. *ACS Sustain. Chem. Eng.* **2021**, *9*, 12100–12108. [CrossRef]
33. Wei, C.; Luo, F.; Zhang, C.; Gao, H.; Niu, J.; Ma, W.; Bai, Y.; Zhang, Z. Voltage window-dependent electrochemical performance and reaction mechanisms of $Na_3V_2(PO_4)_3$ cathode for high-capacity sodium ion batteries. *Ionics* **2019**, *26*, 2343–2351. [CrossRef]
34. Chen, R.; Butenko, D.S.; Li, S.; Li, D.; Zhang, X.; Cao, J.; Ogorodnyk, I.V.; Klyui, N.I.; Han, W.; Zatovsky, I.V. Effects of low doping on the improvement of cathode materials $Na_{3+x}V_{2-x}M_x(PO_4)_3$ (M = Co^{2+}, Cu^{2+}; x = 0.01−0.05) for SIBs. *J. Mater. Chem. A* **2021**, *9*, 17380–17389. [CrossRef]
35. Liu, Y.; Rong, X.H.; Bai, R.; Xiao, R.J.; Xu, C.L.; Zhang, C.; Xu, J.P.; Yin, W.; Zhang, Q.H.; Liang, X.M.; et al. Identifying the intrinsic anti-site defect in manganese-rich NASICON-type cathodes. *Nat. Energy* **2023**, *8*, 1088–1096. [CrossRef]
36. Seshan, V.; Iyngaran, P.; Abiman, P.; Kuganathan, N. Atomic-Scale Study of NASICON Type Electrode Material: Defects, Dopants and Sodium-Ion Migration in NaV(PO). *Physchem* **2024**, *5*, 1. [CrossRef]
37. Xiao, H.; Huang, X.; Ren, Y.; Wang, H.; Ding, J.; Zhou, S.; Ding, X.; Chen, Y. Enhanced sodium ion storage performance of $Na_3V_2(PO_4)_3$ with N-doped carbon by folic acid as carbon-nitrogen source. *J. Alloy. Compd.* **2018**, *732*, 454–459. [CrossRef]
38. Liang, E.J.; Ding, P.; Zhang, H.R.; Guo, X.Y.; Du, Z.L. Synthesis and correlation study on the morphology and Raman spectra of CN_x nanotubes by thermal decomposition of ferrocene/ethylenediamine. *Diam. Relat. Mat.* **2004**, *13*, 69–73. [CrossRef]
39. Aragón, M.J.; Lavela, P.; Ortiz, G.F.; Tirado, J.L. Effect of Iron Substitution in the Electrochemical Performance of $Na_3V_2(PO_4)_3$ as Cathode for Na-Ion Batteries. *J. Electrochem. Soc.* **2015**, *162*, A3077–A3083. [CrossRef]
40. Song, W.; Ji, X.; Yao, Y.; Zhu, H.; Chen, Q.; Sun, Q.; Banks, C.E. A promising $Na_3V_2(PO_4)_3$ cathode for use in the construction of high energy batteries. *Phys. Chem. Chem. Phys.* **2014**, *16*, 3055–3061. [CrossRef]
41. Ishado, Y.; Inoishi, A.; Okada, S. Exploring Factors Limiting Three-Na^+ Extraction from $Na_3V_2(PO_4)_3$. *Electrochemistry* **2020**, *88*, 457–462. [CrossRef]
42. Wang, Q.; Zhang, M.Y.; Zhou, C.G.; Chen, Y.L. Concerted Ion-Exchange Mechanism for Sodium Diffusion and Its Promotion in $Na_3V_2(PO_4)_3$ Framework. *J. Phys. Chem C* **2018**, *122*, 16649–16654. [CrossRef]
43. Saravanan, K.; Mason, C.W.; Rudola, A.; Wong, K.H.; Balaya, P. The First Report on Excellent Cycling Stability and Superior Rate Capability of $Na_3V_2(PO_4)_3$ for Sodium Ion Batteries. *Adv. Energy Mater.* **2012**, *3*, 444–450. [CrossRef]